This is a repository copy of *Synthesis and Ionic Conductivity Studies of In- and Y-Doped Li6Hf2O7 as Solid-State Electrolyte for All-Solid State Li-Ion Batteries*.

White Rose Research Online URL for this paper:
http://eprints.whiterose.ac.uk/147663/

Version: Published Version

Synthesis and Ionic Conductivity Studies of In- and Y-Doped Li₆Hf₂O₇ as Solid-State Electrolyte for All-Solid State Li-Ion Batteries

M. Amores,[a,b] S. A. Corr,[a,z] and E. J. Cussen[b]

[a]*School of Chemistry, University of Glasgow, Glasgow G12 8QQ, United Kingdom*
[b]*Department of Pure and Applied Chemistry, The University of Strathclyde, Glasgow G1 1XL, United Kingdom*

The development of all solid-state lithium batteries is reliant on suitable high performance solid state electrolytes. Here, we present the synthesis and ionic conductivity of the In- and Y-doped $Li_6Hf_2O_7$ materials; $Li_{6+x}Hf_{2-x}M_xO_7$ ($M = In^{3+}$, Y^{3+}). Microwave-assisted synthesis was used to give phase pure material after heating for 4 hours at 850°C. The ionic conductivity of the materials is increased with the insertion of interstitial lithium ion within the structure from 0.02 to 0.25 mS cm⁻¹ at 174°C and the activation energy for ionic conduction is lowered from 0.97(4) eV to 0.42(3) eV with respect to the undoped material.

Conventional lithium-ion batteries provide exceptionally high energy densities, making them the most popular option for mobile/portable applications.[1] Nevertheless, safety issues and limitations on the operating voltages associated with the use of liquid electrolytes as ionic media for Li-ion diffusion between the electrodes, have led to the proposed introduction of all-solid state batteries, where this liquid electrolyte is replaced by a Li-ion solid-state conductor.[2–4] The use of solid-state electrolytes would allow access to higher operating voltages and could address many safety concerns.[2,3] There are several candidate systems as solid-state electrolytes,[5] with four families being the most widely studied: the air stable NASICON-like LiMM'(PO₄)₃ structures,[6] lithium containing garnet materials with ionic conductivity up to 1.3 mS cm⁻¹,[7–10] La₂/₃Li₁/₃TiO₃ perovskites in the same range of conductivities,[11,12] and the most recent thio-LISICON Li₁₀GeP₂S₁₂ materials with conductivities topping the 10 mS cm⁻¹,[13–15] matching those of liquid electrolytes. However, despite achieving ionic conductivities comparable with those of liquid electrolytes, different drawbacks – such as instability at low voltages or large grain-boundary resistances,[16–19] have hampered their full implementation. Thus, the search for new candidate materials remains a challenge for the realization of next generation of Li-ion batteries.

The structure of the Li₆Hf₂O₇ shown in Figure 1 contains Li⁺ ions in 5-fold oxygen coordination in a square pyramid geometry and Hf⁴⁺ ions octahedrally coordinated by oxide. The lithium ions form pair of chains through the structure. This monoclinic phase can be considered as an anion-deficient NaCl rock salt structure with Li⁺ and Hf⁴⁺ ions on the Na⁺ positions and the oxide occupying ⁷/₈ of the anion positions.[20,21] The presence of these vacant positions and the availability of interstitial positions in the structure suggests it should be possible to tailor the lithium stoichiometry in order to modify the ionic conductivity of the material to generate a solid lithium electrolyte.

Non stoichiometry is a well-studied pathway for increasing lithium conductivity in battery materials. This has been studied in cathode materials such as Li$_x$CoO₂,[22] the solid-state electrolyte[23] LiMgPO₄ and the low voltage electrode material LiVO₂.[24] Specifically, the role of interstitial lithium in lithium-rich anti-perovskite has been found to determine the superionic behavior of the material.[25] Thus, the introduction of interstitial lithium ions in the Li₆Hf₂O₇ structure by selective aliovalent doping is expected to increase the lithium ionic conductivity in the material. This is the approach we have undertaken in this work.

The isostructural compound Li₆Zr₂O₇ has been reported by Zocchi et al. in 1993.[26] Increases in the ionic conductivity of this material have been achieved by adding interstitial lithium ions to the structure.[27] The opposite mechanism of vacancy creation has been demonstrated by Rao et al.[28] Most recently, this material has been synthesized in nanofiber form by use of electrospinning techniques to modify the conductivity.[29] The sorption properties of this material has been examined and showed good performance for CO₂ gas capture[30–32] extending interest in this material beyond its ability as an ionic conductor.

We report here the microwave-assisted synthesis of the Li₆Hf₂O₇ material, its aliovalent doping with In³⁺ and Y³⁺ ions to introduce interstitial lithium ions, the structural characterization of these materials and the influence of this doping on the ionic conductivity of these compounds.

Experimental

Synthetic procedures.—All reagents were used as supplied: LiOH·H₂O (98%) from Sigma-Aldrich and HfO₂ (99.99%), In₂O₃ (99.997%) and Y₂O₃ (99.9%) from Alfa Aesar.
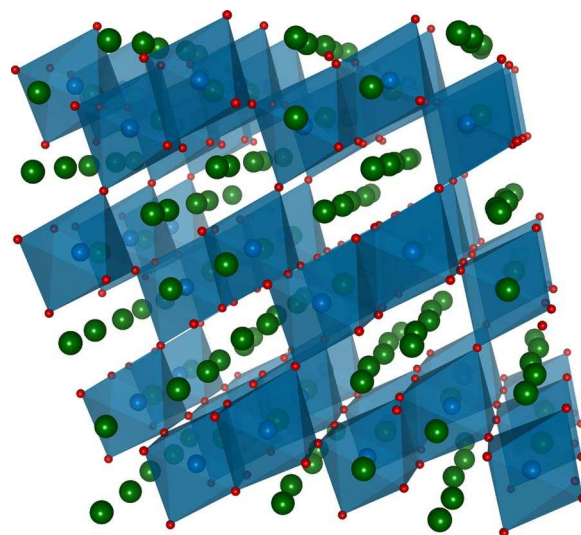
Figure 1. Crystal structure of the Li₆Hf₂O₇ material with C2/c space group of symmetry. Li⁺ ions are shown in green; O²⁻ anions are shown in red and Hf⁴⁺ are shown in blue with their octahedral coordination environment explicitly shown.

[z]E-mail: Serena.Corr@glasgow.ac.uk

For the microwave-assisted solid-state synthesis of the In- and Y-doped $Li_6Hf_2O_7$ materials, stoichiometric amounts of reagents were mixed and ball milled for 20 minutes at 20 Hz with stainless steel milling media. The resulting fine powder was pelleted at 3 tonnes under uniaxial pressure. The pelleted material was heated at 700°C for 6 hours in a 2.45 GHz CEM Phoenix hybrid microwave furnace for the decomposition of the precursor materials. Subsequently, the material was reground and pelleted for a second heat-treatment carried out in air at 850°C for 4 hours in the same microwave furnace with a low heating rate of 2°C min⁻¹ to reduce lithium evaporation. For higher doping levels of x ≥ 0.10 an additional heat-treatment of 850°C for 4 hours was used to increase sample purity.

Structural characterization.—The purity and crystal structures of these samples was assessed using powder X-ray diffraction. A PANalytical X'Pert PRO Diffractometer was used for this purpose using Cu-Kα radiation in the 2θ range 15–60° and a step size of 0.016°. These data were analyzed by Rietveld refinement with the Generalized Structure Analysis System (GSAS),[33] along with the graphical user interface EXPGUI.[34]

Scanning electron microscopy and energy-dispersive X-ray spectroscopy.—Particle size and morphology were examined using scanning electron microscopy (SEM) images acquired with a Phillips XL30 ESEM microscope equipped with an Oxford Instruments Energy 250 energy dispersive spectrometer. Samples were ground and a tiny amount of the fine powder was deposited over a carbon-taped sample holder and gold-coated prior to analysis. Copper tape was employed as an EDX calibration standard and the voltage of the incident beam was 20 keV.

Electrochemical impedance spectroscopy.—Transport measurements were performed on a Solartron 1260 Impedance Analyzer using an *ac rms* voltage of 200 mV in the frequency range of $1–10^6$ Hz and a temperature range between RT and 424°C in 50°C intervals. The as-synthetized powders were cold-pressed under uniaxial pressure at 3 tons and the resultant pellets were heated for 4 hours at 850°C, obtaining 1–2 mm thick pellets with a diameter of 10 mm. Platinum electrodes were connected using a suspension of ca. 1 μm platinum particles on opposing faces of the pellet.

Results and Discussion

Synthesis and structural characterization.—In order to create Li non-stoichiometry on the material, the substitution of Hf^{4+} ion with trivalent ions was undertaken, with the anticipation that charge balance would be maintained by the incorporation of additional Li^+ into the structure. Of the various trivalent ions in the periodic table, In^{3+} and Y^{3+} were the most suitable ions to dope the $Li_6Hf_2O_7$ due to their relatively close ionic radius to Hf^{4+} (In^{3+} = 0.80 Å, Y^{3+} = 0.90 Å and Hf^{4+} = 0.71 Å)[40] together with the redox stability of the ions, required for any solid-state electrolyte for lithium-ion battery applications.

Compositions from the series' $Li_{6+x}Hf_{2-x}In_xO_7$ and $Li_{6+x}Hf_{2-x}Y_xO_7$ were synthesized by a novel microwave-assisted solid-state route we have developed previously for the synthesis of other solid-state electrolyte materials for lithium ion batteries.[8] The use of microwave radiation in solid-state synthesis has been demonstrated as an energy efficient synthetic route which enables the use of lower temperatures and shorter times compared with conventional solid-state synthetic routes.[35] Our synthesis is facilitated by the presence of starting materials, such as the LiOH precursor,[36] that strongly couple with microwaves and with materials with high dielectric constants such as the HfO_2 that can effectively couple with microwave radiations at high temperatures, in a similar way to the ZrO_2 precursor.[37–39]

Undoped $Li_6Hf_2O_7$ and doped compounds up to $x = 0.05$ were obtained as single phase samples at a temperature of 850°C. This re-

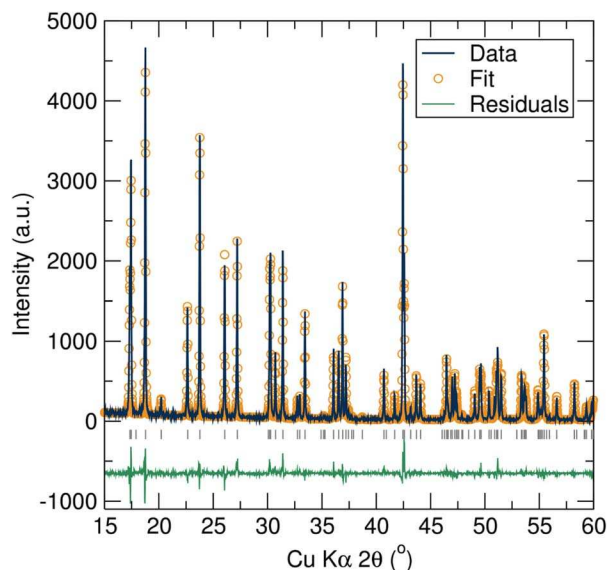**Figure 2.** Rietveld refinement against X-ray diffraction data collected from the undoped $Li_6Hf_2O_7$ material. The monoclinic structure gives a good agreement with the data. R_{wp} = 12.75% and R_p = 9.41%.

quired only four hours for the synthesis compared with several days required by conventional methods previously reported.[20] Due to the dominance of the diffraction profile by the Hf^{4+} cations and the low symmetry of the structure the atomic coordinates and anion occupancies were fixed at the published values. The minimal scattering from Li^+ meant it was not possible to identify the location of the additional Li^+ in the structure. Rietveld refinement of the lattice parameters and profile coefficients shows that this simple approach gives a good agreement between the experimental data and a calculated model for the C2/c space group (Fig. 2). The cell parameters obtained from the Rietveld refinements resulted in a = 10.4157(2) Å b = 5.9678(1) Å and c = 10.1589 (2) Å with a β angle of 100.385(1)° leading to a cell volume of 621.13(2) Å³ for the undoped material.

For higher dopant levels up to $Li_{6.15}Hf_{1.85}In_{0.15}O_7$ and $Li_{6.10}Hf_{1.90}Y_{0.10}O_7$ an additional four hours of heating at 850°C was needed in order to achieve single phase materials. The solubility limit for the In^{3+} doping was identified at concentrations higher than 0.15, when the secondary phase $LiInO_2$ starts to appear and further heating leaded to decomposition of the target material. In the case of the Y^{3+} doping the solubility limit is reached just above x(Y) = 0.10, with appearance of additional peaks at this composition. These peaks could not be indexed by a reduction in space group symmetry, nor do they arise from any of the starting materials or obvious binary or ternary oxides that may result in this system. The lower solubility of this cation in the structure is presumably due to the larger deviation from the radius of Li^+ exhibited by Y^{3+} compared to Hf^{4+}.

Inspection of the diffraction patterns shown in Figure 3 shows no gross changes in the Bragg scattering suggesting the structure is largely unchanged. It should be clearly understood that due to the negligible X-ray scattering arising from Li^+ in the presence of the dominant scatterer Hf^{4+} these data give no insight into the placement of the additional lithium in the structure. It may be assumed that Li^+ exists at interstitial sites, but this remains conjecture at this stage.

There are no dramatic changes in the structures derived from Rietveld analyses, with the most significant being a decrease in the monoclinic distortion with Y^{3+} doping as manifested in the β lattice parameter shown in Figure 4. In the case of the In^{3+} doping, there were no significant changes in the structure. Again, these results are as anticipated after consideration of the ionic radii of In^{3+}, 0.80 Å, and Hf^{4+}, 0.71 Å, and comparison with the radius of Li^+ 0.76.[40]

EDX analyses of $Li_{6.15}Hf_{1.85}In_{0.15}O_7$ and $Li_{6.10}Hf_{1.90}Y_{0.10}O_7$ estimated the relative atomic ratios of In:Hf as 0.09 and Y:Hf = 0.05
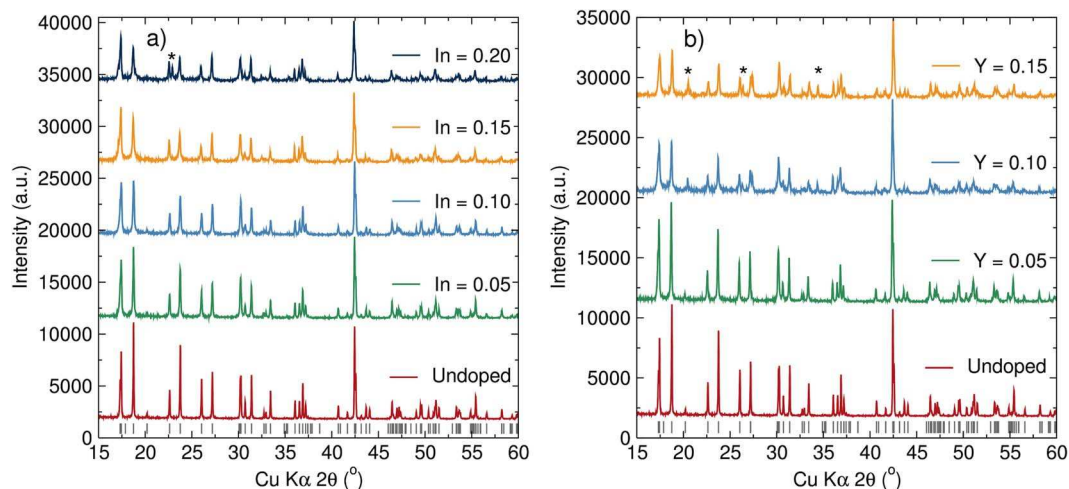
Figure 3. Diffraction patterns collected from the (a) $Li_{6+x}Hf_{2-x}In_xO_7$ and (b) $Li_{6+x}Hf_{2-x}Y_xO_7$. The peaks arising from impurity phases at the highest dopant levels are indicated.

which are in good agreement with the values of 0.09 and 0.04 that are anticipated from the targeted stoichiometries.

A powdered sample of $Li_6Hf_2O_7$ shows agglomerates of microparticles between 10 and 50 microns with no specific morphology as shown in Figure 5. A fractured pellet for the $Li_{6.15}Hf_{1.85}In_{0.15}O_7$ mate-

rial shows large grains with good connection between them. Despite that, the density of this material was only ≈78% of the theoretical density. Further sintering at higher temperatures in order to achieve higher densities resulted in decomposition of the material, possibly due to lithium evaporation.

An elemental compositional map was generated from a cracked pellet of the material that showed the highest conductivity, $Li_{6.10}Hf_{1.90}Y_{0.10}O_7$. Figure 6 shows that this map indicated a uniform distribution of Hf, Y and O across the pellet without any apparent segregation or inhomogeneity.

Ionic conductivity behavior.—The ionic transport properties of the undoped and doped materials were analyzed by means of impedance analysis and a typical Nyquist plot for the undoped material at 174°C is shown in Figure 7. A clear semicircle is observed at higher frequencies due to intra-grain ionic conductivity. The linear lower frequency response is typical of the blocking of Li^+ due to the use of platinum electrodes, indicating the ionic nature of the impedance. In order to obtain the value for the resistance of the material, these data were fitted using an equivalent circuit of a resistor, due to the resistance to ionic conduction, with a parallel constant phase element due to double layer polarization. The capacitance resulting from the fit is in the order of 10^{-12} F, indicating the observed
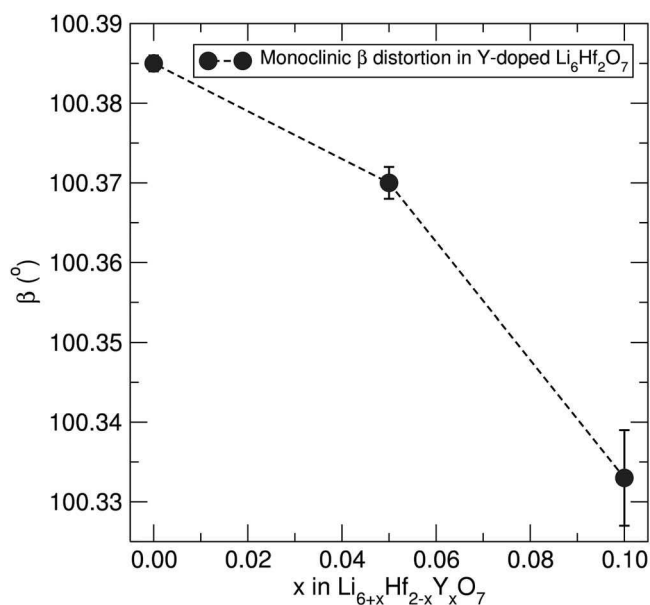

Figure 4. Monoclinic distortion (β-angle) variation following the substitution of Hf^{4+} ions with Y^{3+}. A progressive decrease is observed due to the bigger size of the Y^{3+} ions compared to Hf^{4+}.
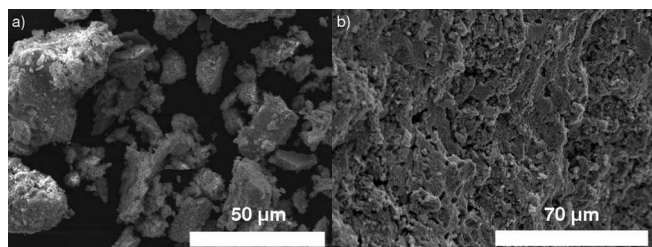

Figure 5. SEM image of (a) the as-synthesized $Li_6Hf_2O_7$ and (b) the pelleted $Li_{6.15}Hf_{1.85}In_{0.15}O_7$ material prepared for EIS analyses.
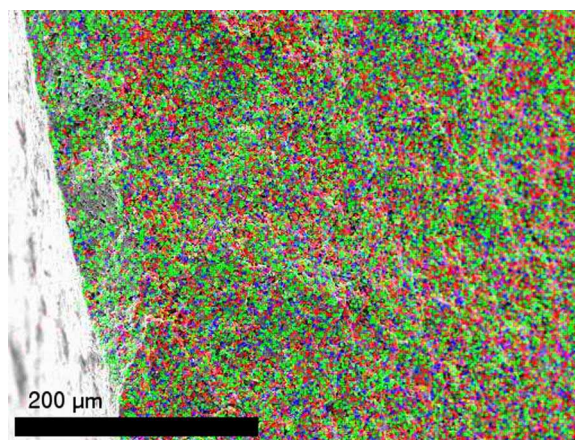

Figure 6. An elemental map of the Hf, Y and O distributions on a fractured pellet that had been studied by impedance analysis. This is generated from EDX measurements and false colored to indicate the contributions from Hf (green), Y (blue) and O (red).
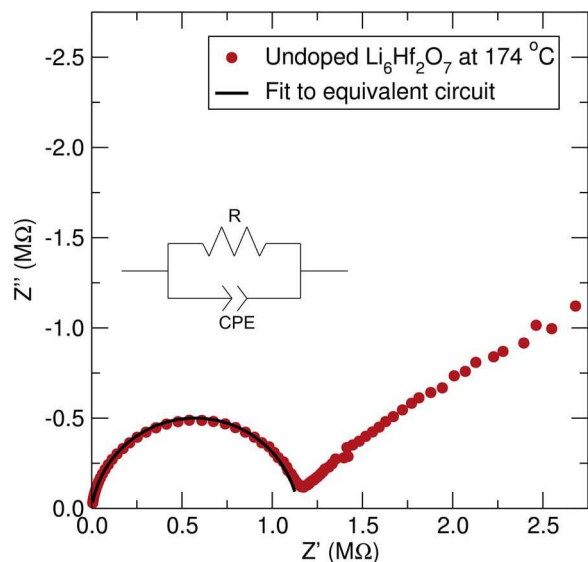
Figure 7. Nyquist plot of the impedance data for $Li_6Hf_2O_7$ at 174°C (red dots) and the fit derived from the proposed electrical circuit (solid black line) of a parallel arrangement of resistor (R) and constant phase element (CPE).

resistance is mainly due to bulk conductivity,[41] and the conductivity is 1.95×10^{-2} mS cm^{-1}.

In order to obtain further information about the ionic conduction phenomena in these materials, the activation energies of all the phase

pure compositions were determined by variable temperature conductivity measurements. Arrhenius analysis of the data from the undoped material is shown in Figure 8. This indicates that the activation energy for ionic diffusion in $Li_6Hf_2O_7$, 0.97(4) eV, which lies between the values reported for the isostructural $Li_6Zr_2O_7$ by Goodenough and co-workers[27] of 0.84 eV and the 1.25 eV obtained by Rao et al.[28] Since there is more than one variable parameter within each study (e.g., synthetic conditions, density, set-up employed on the measurements, etc.), it is difficult to draw direct comparisons based on these values alone. Also, the activation barrier presented here represents the total conductivity which is highly dependent on the sample microstructure. A detailed study between both isostructural families of materials would be required in order to provide a better understanding regarding the role of the Hf and Zr atoms in the ionic conductivity of these materials.

For the In doped material, the ionic conduction at 174°C is progressively enhanced with the insertion of the In^{3+} dopant, until it is increased by one order of magnitude at 174°C for the x(In) = 0.15. The activation energy for ionic conductivity is decreased by a 28% compared to the undoped parent material. In all the cases the evolution of ionic conductivity with temperature agrees accurately with an Arrhenius behavior as shown in Figure 8.

The introduction of Y^{3+} also increased the ionic conductivity proportionally to Y^{3+} doping stoichiometry as shown in Figure 9, again giving an order of magnitude higher for the x(Y) = 0.10 composition at 174°C. Due to the increased ionic conductivity, for the Y-doped material, reliable data could be acquired at room temperature. The activation energy is significantly altered by this doping reaching a value as low as 0.42(3) eV for the x(Y) = 0.10 composition as shown in Figure 9. The transport properties of all of these compounds are collected in Table I and Figure 10.
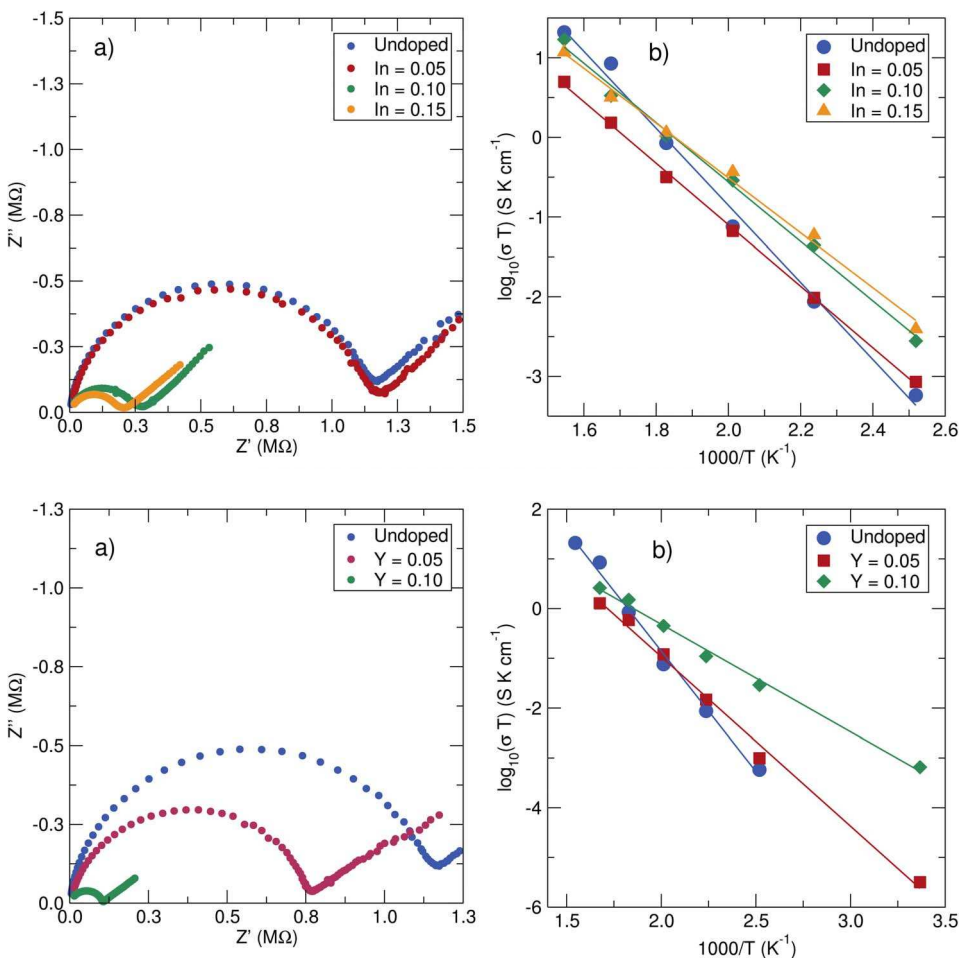

Figure 8. Nyquist plot of the impedance spectra of the In-doped family at 174°C (a) and Arrhenius plot of the conductivity measured over the 124 to 424°C temperature range (b).

Figure 9. Nyquist plot of (a) the impedance of the $Li_{6+x}Hf_{2-x}Y_xO_7$ compounds at 174°C and (b) the values of conductivity derived in the range $20 \leq T /°C \leq 424$.

Table I. Ionic conductivity and activation energy data for $Li_{6+x}Hf_{2-x}In_xO_7$ and $Li_{6+x}Hf_{2-x}Y_xO_7$.

Compound	Ionic Conductivity at 174°C (mS cm^{-1})	Activation Energy (eV)
$Li_{6.00}Hf_{2.00}O_7$	1.95×10^{-2}	0.97(4)
$Li_{6.05}Hf_{1.95}In_{0.05}O_7$	2.17×10^{-2}	0.77(1)
$Li_{6.10}Hf_{1.90}In_{0.10}O_7$	9.88×10^{-2}	0.74(3)
$Li_{6.15}Hf_{1.85}In_{0.15}O_7$	1.33×10^{-1}	0.68(3)
$Li_{6.05}Hf_{1.95}Y_{0.05}O_7$	3.28×10^{-2}	0.68(2)
$Li_{6.10}Hf_{1.90}Y_{0.10}O_7$	2.46×10^{-1}	0.42(3)

Table II. Values of the frequency exponent n for the $Li_{6+x}Hf_{2-x}In_xO_7$ and $Li_{6+x}Hf_{2-x}Y_xO_7$ materials.

Compound	n exponent value
$Li_{6.00}Hf_{2.00}O_7$	1.29(1)
$Li_{6.05}Hf_{1.95}In_{0.05}O_7$	1.23(1)
$Li_{6.10}Hf_{1.90}In_{0.10}O_7$	0.93(2)
$Li_{6.15}Hf_{1.85}In_{0.15}O_7$	0.94(1)
$Li_{6.05}Hf_{1.95}Y_{0.05}O_7$	1.07(2)
$Li_{6.10}Hf_{1.90}Y_{0.10}O_7$	0.80(2)

In the absence of structural information on the location of the additional Li$^+$ inserted into the material it is only possible to speculate on the origin of this decrease in activation energy. If interstitial Li$^+$ is introduced then a step change in activation energy would be expected due to the introduction of a new pathway for Li$^+$ migration. The more gradual trend observed here suggests that increasing values of x may be causing incremental increases in electrostatic repulsion and destabilising Li$^+$ and so reducing the barrier to ion motion.

The relationship of the conductivity with the frequency is shown in Figure 11 and displays two clear behaviors as the frequency is varied. At low to intermediate frequencies the conductivity is approximately constant due to the dominance of the jump relaxation of Li ions by dc conductivity, leading to a plateau-like region on the graph. This region displays a slight curvature at very low frequencies due to the polarization arising from the increasing resistance to lithium diffusion at the Li-blocking Pt electrodes when decreasing the frequency of the ac field. The second region at higher frequencies indicates a rapid increase in charge transport that can be attributed to the forward and backward movements of the ions under the influence of the rapid ac field.[42–44]

This behavior is in agreement with the Jonscher universal power law[45] (Eq. 1) presenting both of the components, the σ_{dc} corresponding to the plateau region and the linear region corresponding to the f^n – multiplied by a proportionality constant A. The value for conductivity in the plateau region is increased as the doping concentration increases, indicating the positive impact on the ionic conductivity of the dopant ions.

$$\sigma(f) = \sigma_{dc} + Af^n \qquad [1]$$

The frequency exponent n has been calculated from fits of the frequency dependent range. The variation of the n exponent with respect to the doping (Table II) is clear, where a decrease in the n exponent with increasing amount of the dopant is observed indicating a lower contribution of the forward-backward jumps in favor of macroscopic ionic diffusion. These values for the n exponent are close to unity, similar to the values reported for other crystalline lithium ion conductor materials, such as the Li-NASICON structures.[46]
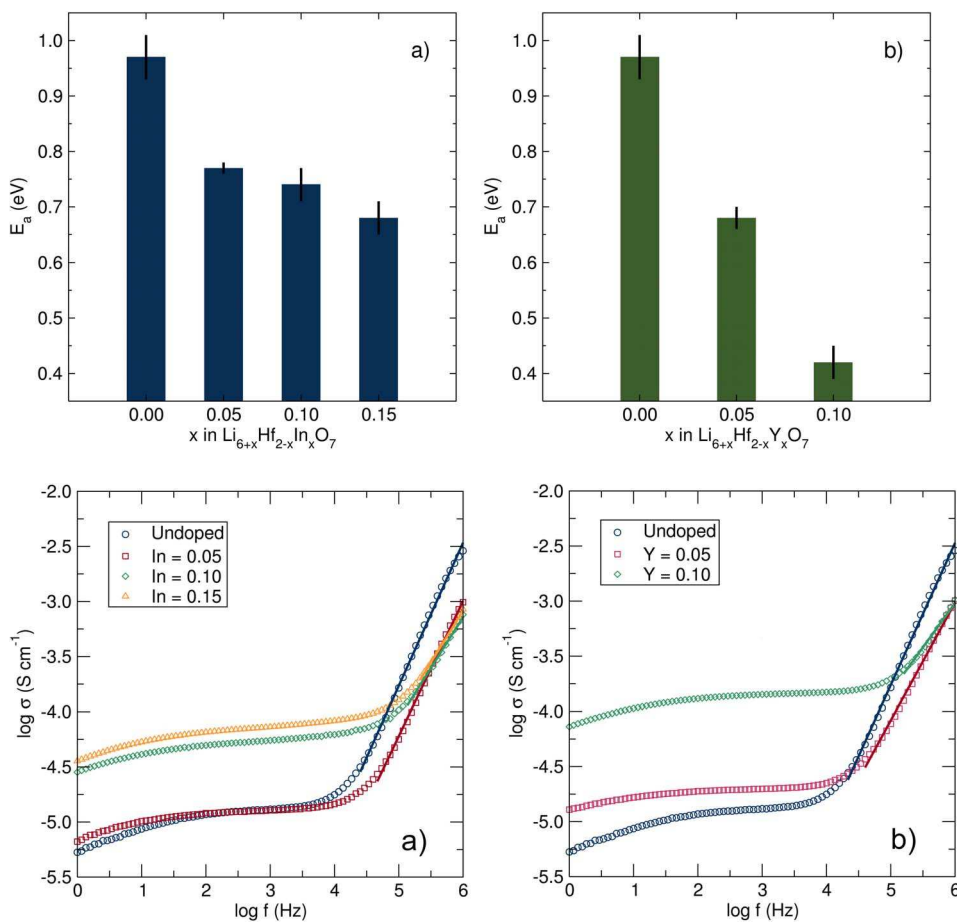
Figure 10. Activation energy for ionic diffusion as calculated from Arrhenius fitting for the different levels of In (a) and Y doping (b) of the $Li_7Hf_6O_7$ material. A clear decrease is observed with increasing amount of dopant.

Figure 11. Ionic conductivity of the (a) In- and (b) Y-doped $Li_6Hf_2O_7$ materials as a function of the frequency measured for the different amounts of dopant. Fits to the frequency dependent range data are indicated by a solid line of the same color as the fitted data set.

Conclusions

We have demonstrated the successful synthesis and characterization of $Li_6Hf_2O_7$ by an energy-efficient microwave-assisted synthetic approach. An aliovalant doping strategy has been employed using Y^{3+} and In^{3+} to increase the number of lithium per formula unit, and so improve the ionic conductivity of the material. Powder X-ray diffraction has been used to follow the dopant insertion within the crystal structure. In this manner, it was found that the upper solubility limits of the dopants is $x(In) = 0.15$ for $Li_{6+x}Hf_{2-x}In_xO_7$ and $x(Y) = 0.10$ for $Li_{6+x}Hf_{2-x}Y_xO_7$. The ionic conductivity of the phase pure materials has been studied by means of impedance spectroscopy, showing a decrease of the energy barrier for ionic conductivity from 0.97 eV for the undoped material to 0.62 eV for the 0.15 In-doped material and a value of 0.42 eV for the 0.10 Y-doped compound. This low value compares favorably to other promising solid-state electrolyte materials.[47] This demonstrates the potential of disorder in relatively simple crystal structures to generate new materials for solid-state electrolytes applications.

Acknowledgments

References

1. J. M. Tarascon and M. Armand, *Nature*, **414**(6861), 359 (2001).
2. X. Y. Yao, B. X. Huang, J. Y. Yin, G. Peng, Z. Huang, C. Gao, D. Liu, and X. X. Xu, *Chin. Phys. B*, **25**(1), 018802 (2016).
3. K. Takada, *Acta Mater.*, **61**(3), 759 (2013).
4. J. Janek and W. G. Zeier, *Nat. Energy*, **1**(9), 16141 (2016).
5. P. Knauth, *Solid State Ionics*, **180**(14–16), 911 (2009).
6. N. Anantharamulu, K. Koteswara Rao, G. Rambabu, B. Vijaya Kumar, V. Radha, and M. Vithal, *J. Mater. Sci.*, **46**(9), 2821 (2011).
7. C. Bernuy-Lopez, W. Manalastas, J. M. Lopez del Amo, A. Aguadero, F. Aguesse, and J. A. Kilner, *Chem. Mater.*, **26**(12), 3610 (2014).
8. M. Amores, T. E. Ashton, P. J. Baker, E. J. Cussen, and S. A. Corr, *J. Mater. Chem. A*, **4**(5), 1729 (2016).
9. R. Inada, S. Yasuda, M. Tojo, K. Tsuritani, T. Tojo, and Y. Sakurai, *Front. Energy Res.*, **4**(28), (2016).
10. V. Thangadurai, S. Narayanan, and D. Pinzaru, *Chem. Soc. Rev.*, **43**(13), 4714 (2014).
11. X. Lin, H. Wang, H. Du, X. Xiong, B. Qu, Z. Guo, and D. Chu, *ACS Appl. Mater. Interfaces*, **8**(2), 1486 (2016).
12. C. Ma, Y. Q. Cheng, K. Chen, J. C. Li, B. G. Sumpter, C. W. Nan, K. L. More, N. J. Dudney, and M. F. Chi, *Adv. Energy Mater.*, **6**(11), 1600053 (2016).
13. Y. Kato, S. Hori, T. Saito, K. Suzuki, M. Hirayama, A. Mitsui, M. Yonemura, H. Iba, and R. Kanno, *Nat. Energy*, **1**, 16030 (2016).
14. R. Kanno, T. Hata, Y. Kawamoto, and M. Irie, *Solid State Ionics*, **130**(1–2), 97 (2000).
15. N. Kamaya, K. Homma, Y. Yamakawa, M. Hirayama, R. Kanno, M. Yonemura, T. Kamiyama, Y. Kato, S. Hama, K. Kawamoto, and A. Mitsui, *Nat. Mater.*, **10**(9), 682 (2011).
16. W. D. Richards, L. J. Miara, Y. Wang, J. C. Kim, and G. Ceder, *Chem. Mater.*, **28**(1), 266 (2016).
17. S. Wenzel, S. Randau, T. Leichtweiss, D. A. Weber, J. Sann, W. G. Zeier, and J. Janek, *Chem. Mater.*, **28**(7), 2400 (2016).
18. Y. S. Jung, D. Y. Oh, Y. J. Nam, and K. H. Park, *Isr. J. Chem.*, **55**(5), 472 (2015).
19. A. C. Luntz, J. Voss, and K. Reuter, *J. Phys. Chem. Lett.*, **6**(22), 4599 (2015).
20. R. Czekalla and W. Jeitschko, *Z. Anorg. Allg. Chem.*, **619**(12), 2038 (1993).
21. I. Abrahams, P. Lightfoot, and P. G. Bruce, *J. Solid State Chem.*, **104**(2), 397 (1993).
22. A. Van der Ven and G. Ceder, *J. Power Sources*, **97–98**, 529 (2001).
23. L. Enciso-Maldonado, M. S. Dyer, M. D. Jones, M. Li, J. L. Payne, M. J. Pitcher, M. K. Omir, J. B. Claridge, F. Blanc, and M. J. Rosseinsky, *Chem. Mater.*, **27**(6), 2074 (2015).
24. A. R. Armstrong, C. Lyness, P. M. Panchmatia, M. S. Islam, and P. G. Bruce, *Nat. Mater.*, **10**(3), 223 (2011).
25. R. Mouta, E. M. Diniz, and C. W. A. Paschoal, *J. Mater. Chem. A*, **4**(5), 1586 (2016).
26. M. Zocchi, I. N. Sora, L. E. Depero, and R. S. Roth, *J. Solid State Chem.*, **104**(2), 391 (1993).
27. Y. Liao, P. Singh, K.-S. Park, W. Li, and J. B. Goodenough, *Electrochim. Acta*, **102**, 446 (2013).
28. R. P. Rao, M. V. Reddy, S. Adams, and B. V. R. Chowdari, *Mater. Sci. Eng., B*, **177**(1), 100 (2012).
29. Y. L. Liu and X. F. Hua, *Int. J. Appl. Ceram. Technol.*, **13**(3), 579 (2016).
30. Y. Duan and J. Lekse, *PCCP*, **17**(35), 22543 (2015).
31. X.-S. Yin, S.-P. Li, Q.-H. Zhang, and J.-G. Yu, *J. Am. Ceram. Soc.*, **93**(9), 2837 (2010).
32. H. Pfeiffer and P. Bosch, *Chem. Mater.*, **17**(7), 1704 (2005).
33. A. C. Larson and R. B. Von Dreele, *Los Alamos National Laboratory Report LAUR* 86, (1994).
34. B. H. Toby, *J. Appl. Crystallogr.*, **34**, 210 (2001).
35. H. J. Kitchen, S. R. Vallance, J. L. Kennedy, N. Tapia-Ruiz, L. Carassiti, A. Harrison, A. G. Whittaker, T. D. Drysdale, S. W. Kingman, and D. H. Gregory, *Chem. Rev.*, **114**(2), 1170 (2014).
36. W. G. Hennig, W. A. G. Voss, J. M. Dubowik, J. W. Piche, R. Griffiths, R. F. Kovar, and H. K. Kua, Google Patents, 1991.
37. J. Robertson, *Eur. Phys. J. Appl. Phys.*, **28**(3), 265 (2004).
38. J. Lasri, P. D. Ramesh, and L. Schächter, *J. Am. Ceram. Soc.*, **83**(6), 1465 (2000).
39. J. De Roo, K. De Keukeleere, J. Feys, P. Lommens, Z. Hens, and I. Van Driessche, *J. Nanopart. Res.*, **15**(7), 1 (2013).
40. R. Shannon, *Acta Cryst.*, **A32**(5), 751 (1976).
41. J. T. S. Irvine, D. C. Sinclair, and A. R. West, *Adv. Mater.*, **2**(3), 132 (1990).
42. K. Funke, *Solid State Ionics*, **94**(1), 27 (1997).
43. J. C. Dyre, *J. Appl. Phys.*, **64**(5), 2456 (1988).
44. K. Funke, *Prog. Solid State Chem.*, **22**(2), 111 (1993).
45. A. K. Jonscher, *Nature*, **267**(5613), 673 (1977).
46. C. J. Leo, G. V. Subba Rao, and B. V. R. Chowdari, *J. Mater. Chem.*, **12**, 1848 (2002).
47. J. C. Bachman, S. Muy, A. Grimaud, H. H. Chang, N. Pour, S. F. Lux, O. Paschos, F. Maglia, S. Lupart, P. Lamp, L. Giordano, and Y. Shao-Horn, *Chem. Rev.*, **116**(1), 140 (2016).